Edited by Gustaaf Van Tendeloo, Dirk Van Dyck, and Stephen J. Pennycook

Handbook of Nanoscopy

Volume 1

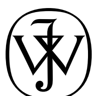

WILEY-VCH Verlag GmbH & Co. KGaA

The Editors

Prof. Gustaaf Van Tendeloo
Univ. of Antwerp (RUCA)
EMAT
Groenenborgerlaan 171
2020 Antwerp
Belgium

Prof. Dirk Van Dyck
Univ. of Antwerp (RUCA)
EMAT
Groenenborgerlaan 171
2020 Antwerp
Belgium

Prof. Dr. Stephen J. Pennycook
Oak Ridge National Lab.
Condensed Matter Science Div.
Oak Ridge, TN 37831-6030
USA

All books published by **Wiley-VCH** are carefully produced. Nevertheless, authors, editors, and publisher do not warrant the information contained in these books, including this book, to be free of errors. Readers are advised to keep in mind that statements, data, illustrations, procedural details or other items may inadvertently be inaccurate.

Library of Congress Card No.: applied for

British Library Cataloguing-in-Publication Data
A catalogue record for this book is available from the British Library.

Bibliographic information published by the Deutsche Nationalbibliothek
The Deutsche Nationalbibliothek lists this publication in the Deutsche Nationalbibliografie; detailed bibliographic data are available on the Internet at <http://dnb.d-nb.de>.

© 2012 Wiley-VCH Verlag & Co. KGaA, Boschstr. 12, 69469 Weinheim, Germany

All rights reserved (including those of translation into other languages). No part of this book may be reproduced in any form – by photoprinting, microfilm, or any other means – nor transmitted or translated into a machine language without written permission from the publishers. Registered names, trademarks, etc. used in this book, even when not specifically marked as such, are not to be considered unprotected by law.

Cover Design Adam-Design, Weinheim
Typesetting Laserwords Private Limited, Chennai, India
Printing and Binding betz-druck GmbH, Darmstadt

Printed in the Federal Republic of Germany
Printed on acid-free paper

Print ISBN: 978-3-527-31706-6
ePDF ISBN: 978-3-527-64188-8
oBook ISBN: 978-3-527-64186-4
ePub ISBN: 978-3-527-64187-1
Mobi ISBN: 978-3-527-64189-5

3
Ultrahigh-Resolution Transmission Electron Microscopy at Negative Spherical Aberration

Knut W. Urban, Juri Barthel, Lothar Houben, Chun-Lin Jia, Markus Lentzen, Andreas Thust, and Karsten Tillmann

3.1
Introduction

With the realization of the Rose-corrector, the old dream of electron optics to be able to construct spherical-aberration-corrected lens systems has come true [1–3]. Aberration-corrected transmission electron microscopy offers a great variety of new or expanded research opportunities for physics, chemistry, and materials science. Of these, a prominent field is that of investigations in atomic dimensions. With certain exceptions, most of the earlier high-resolution work was carried out in conventional noncorrected instruments, in spite of the fact that the images looked like atomic, was in reality not truly atomically resolving. Owing to aberration-induced contrast delocalization, a given atomic column does also contribute intensity to the positions of neighboring columns in the image. As a consequence, atomic concentrations and lateral shifts on the scale of an individual atomic column could not be measured. In most cases the images merely showed the crystallographic *structure* of a sample; this means a collective *nonlocal* property. Today things have changed; genuine atomic resolution has become available, allowing measurement of individual atomic properties. However, in order to exploit the new possibilities, investigations have to become more quantitative, much beyond the level that appeared sufficient in pre-aberration correction times. But it is worth making the effort: aberration-corrected transmission electron microscopy allows us to measure atomic positions and lateral shifts with close to picometer precision. This changes the electron microscope from a predominantly structure-oriented tool into a physical measurement instrument.

A prominent part in this progress from conventional high-resolution to ultrahigh-resolution work is played by the improvement of both image contrast

Handbook of Nanoscopy, First Edition. Edited by Gustaaf Van Tendeloo, Dirk Van Dyck, and Stephen J. Pennycook.
© 2012 Wiley-VCH Verlag GmbH & Co. KGaA. Published 2012 by Wiley-VCH Verlag GmbH & Co. KGaA.

as well as signal to noise ratio achievable by employing aberration-corrected optics. The common reference for high-resolution microscopy is Scherzer's phase-contrast theory [4]. Formulated at a time when, at a fixed value of the objective-lens spherical aberration parameter, the only variable to optimize contrast was the objective-lens focal length, this theory provides a value for the lens defocus, yielding optimal contrast up to a certain optical resolution (Scherzer resolution). Unfortunately, the Scherzer focus setting leads to a rather high value of contrast delocalization, higher than the value of the Scherzer resolution itself [5, 6]. This dramatically limits the practical value of Scherzer's conditions. Take a crystal, the lattice parameter of which is just large enough to image, for a given Scherzer resolution, the atom columns separately. In this case, the actual information supplied by the image for a given atom column is rather limited and unspecific. The reason is that the intensity at the position of this column is the sum of its own intensity plus the intensity of the delocalized images of the neighboring columns at this position. Although this may be tolerable for work in which one is interested only in the crystallographic structure, it is totally inadequate for genuine atomic resolution. In microscopes equipped with aberration-correctors, in addition to defocus aberration, the other symmetric aberrations, the spherical aberration of third and fifth order, can be treated as variables suited to optimize contrast not only for optimal resolution but also for minimal contrast delocalization [6, 7]. This is one of the great advantages of aberration-corrected transmission electron microscopy.

Scherzer's theory [4] and also Lentzen's contrast theory for aberration-corrected instruments [7] are linear theories assuming ideally weak objects. However, in materials science most objects are strong scatterers. The possibility to adjust the spherical aberration including the sign allows tackling the problem that the nonlinear terms in treatments for stronger objects make a contribution of opposite sign thus in effect weakening the contrast. This can be considered a second substantial advantage of transmission electron microscopes with aberration-correcting optics and provides the background for the negative spherical-aberration imaging (NCSI) technique discovered by Jia in 2001. NCSI offers substantially sharper contrast maxima, and it proved to be particularly advantageous for imaging low-nuclear-charge light atom species close to heavy atoms [8].

This section is organized as follows. In Section 3.2, the principles of atomic imaging, including NCSI, is treated first. An extra section, Section 3.3, is dedicated to the numerical inversion of the imaging process as a prerequisite for ultrahigh-resolution work. This is followed, in Section 3.4, by a theoretical case study of $SrTiO_3$, in which the key features of NCSI are compared to imaging with positive spherical aberration. In Section 3.5, following a guide to the literature, measurement of the atom positions in ferroelectric 180° inversion domain walls in lead zirconate titanate (PZT) will be treated as an example of the ultrahigh-resolution application of NCSI. The research opportunities that opened up for materials science by atomic-resolution studies employing the NCSI technique have been reviewed by Urban [9, 10] and by Urban *et al.* [11, 12].

3.2 The Principles of Atomic-Resolution Imaging

3.2.1 Resolution and Point Spread

The goal of atomic-resolution work is to measure the set of individual atom positions in a sample $\mathbf{X} = \{\mathbf{r}_1, \mathbf{r}_2, \mathbf{r}_3, \ldots\}$. We are treating here the case of a crystalline sample. We employ an electron wave field represented for simplicity by a single plane wave

$$\psi_0(\mathbf{r}) = \exp(2\pi i \mathbf{k}_0 \cdot \mathbf{r}) \tag{3.1}$$

incident on the upper sample surface. Here, $\mathbf{k}_0$ denotes the wave vector whose modulus is the inverse of the electron wave length λ; $\mathbf{r}$ denotes the general position vector. On its way through the specimen, this wave field interacts with the atomic potential $V(\mathbf{r})$. At electron energies of typically 200–300 keV, the electron wave function $\psi(\mathbf{r})$ in the crystal is given as a solution of the Dirac equation subject to the boundary conditions at the surface. In a small-angle scattering approximation, spin polarization can be neglected and the equation adopts a Schrödiger-type form with relativistically corrected mass and wavelength [13–15].

The wave function at the lower plane of the specimen, the exit-plane wave function ψ_e, contains all the information on the specimen that the electrons can supply us with. In the general case, this information is not directly accessible but encoded in a complicated way determined by the quantum mechanical interaction. In the potential-free space, the exit-plane wave field can be described as a superposition of plane waves. Written as a Fourier integral we thus obtain

$$\psi(\mathbf{r}) = \int\limits_{\mathbf{g}} \psi(\mathbf{g}) \exp\left(2\pi i \mathbf{g} \cdot \mathbf{r}\right) \mathrm{d}\mathbf{g} \tag{3.2}$$

with the modulus of the reciprocal vector $\mathbf{g}$ representing the spatial frequency. This wave field is then the object of the objective lens of the microscope. The intensity distribution in the image plane is given by an equivalent to the Poynting vector, which, again in a small-angle approximation, is proportional to the electron probability density, that is, the absolute square of the wave function,

$$I(\mathbf{r}) \propto \frac{ih}{4\pi m}\left(\psi \nabla \psi^* - \psi^* \nabla \psi\right) \propto \psi^* \psi \tag{3.3}$$

where h is Planck's constant and m is the relativistically corrected electron mass.

If the lens has optical aberrations, these have the effect that the individual components $\psi(\mathbf{g})$ of the exit-plane wave function are multiplied by the phase factor

$$\exp\left(-2\pi i \chi(\mathbf{g})\right) \tag{3.4}$$

where

$$\chi(\mathbf{g}) = \tfrac{1}{2} Z \lambda \mathbf{g}^2 + \tfrac{1}{4} C_S \lambda^3 \mathbf{g}^4 + \ldots \tag{3.5}$$

is the wave-aberration function (expressions comprising up the fifth-order aberration terms can be found in Refs. [3, 16, 17]). The first term is the lens defocus aberration, with Z denoting the defocus parameter [13].[1] The second term is due to third-order spherical aberration, where C_S is the spherical aberration parameter.

The presence of aberrations has the consequence that a point in the object is not imaged into a sharp corresponding point in the image plane but rather into an error or point-spread disk whose radius is given by the point spread function, which also characterizes contrast delocalization

$$R = \max\left|\frac{\partial \chi}{\partial g}\right| = \max\left|Z\lambda g + C_S\lambda^3 g^3 + \ldots\right|, g \text{ in } [0;\ g_{max}] \tag{3.6}$$

where the maximum has to be taken over the whole range of spatial frequencies, up to g_{max}, contributing to the image [13, 6, 18]. In the fully aberration-corrected case, point spread becomes zero. Any finite values of Z and C_S (e.g., applied when taking focal series or for optimizing contrast) will lead to finite values of R. However, as shown below, the values of R can be kept sufficiently small, not to affect most practical high-resolution work.

3.2.2
Contrast

Because numerical solutions of the quantum mechanical scattering problem can now be readily obtained on a computer and comfortable software packages are available (e.g., [19, 20]), contrast should be discussed on the basis of a state-of-the art numerical treatment. That in the following we nevertheless start with the classical approach to treat the simplified cases of weak phase and weak amplitude objects serves a schematic understanding of contrast formation. On the other hand, such a discussion also allows us to point out the severe limitations of such treatments.

We start the discussion with phase contrast. This means that access to the specimen structure is obtained by exploiting the information contained in the locally varying phase of the exit-plane wave field. As in light microscopy, under Zernike phase-contrast conditions [21, 22], the problem arises that the atomic phase contrast has to be converted into amplitude contrast. While in light microscopy the phase shifts are small, the phase shifts in electron microscopy, depending on atomic number and specimen thickness, can be quite large. Nevertheless, for the sake of illustration we apply for the moment the weak phase object approximation (WPO).

1) We follow here the usual sign convention based on a consideration of the phase at a fixed position of the image plane. If the excitation of the objective lens is weakened compared to the ideal value appertaining to the Gaussian focus f_0, the lens is called *underfocused* and the focal length increases to become $f = f_0 + \Delta f$. If the specimen to lens distance is left unchanged, the phase in the image plane is less advanced compared to the Gaussian case, and the defocus parameter Z in Eq. (3.5) adopts a negative value. In this case, a (hypothetical) focused image would be formed behind the fixed image plane. If the excitation of the lens is increased, the lens is said to be *overfocused*, its focal length becomes shorter (Δf is negative), and the focused image would occur in front of the fixed image plane. As a consequence, the phase in the image plane is advanced and Z adopts a positive value.

The conditions can be illustrated schematically in the Gaussian complex number plane. The incident wave is characterized by a vector along the real axis. The diffracted wave is represented by a short vector along the imaginary axis, taking account the fact that the basic physical phase shift of a diffracted wave is $\pi/2$ with respect to the incident wave. The sum of both is a vector rotated in mathematically positive direction by a small angle but of essentially the same amplitude as that of the incident wave. In light microscopy, an additional $\pi/2$ phase shift is imposed on the scattered wave by the so-called $\lambda/4$ plate. Now, summing up yields a shorter resulting vector and a corresponding intensity reduction. As a result, the scattering regions give dark contrast on a bright background. This is called *positive phase contrast* [14].

Phase contrast is governed by the phase-contrast transfer function (PCTF) $\sin 2\pi\chi(\mathbf{g})$, and the spatial-frequency-dependent phase-shifting properties of the lens aberration function can be exploited to produce an equivalent to the Zernike phase plate. Scherzer's optimized PCTF is displayed in Figure 3.1a for an uncorrected instrument. The corresponding PCTF for an aberration-corrected instrument (Figure 3.1b), still maintaining the WPO approximation, was derived by Lentzen *et al.* [6], taking advantage of the fact that now the defocus and the third-order spherical aberration are available for optimization of χ. How this optimization is done depends on the preferences. First of all, we want to eliminate the contrast oscillations between g_S and g_I. Here, g_S is the spatial frequency corresponding to Scherzer's point resolution, and g_I denotes the spatial frequency marking the information limit determined by partial temporal coherence of the illumination system. This in turn is limited by the energy spread of the electron source and by fluctuations of the electron energy and the objective lens current [23, 24]. The second goal is to reduce point spread to a fraction of g_I^{-1}. Finally, we have to take care that the low-contrast (poor-transfer) region at small spatial frequencies is

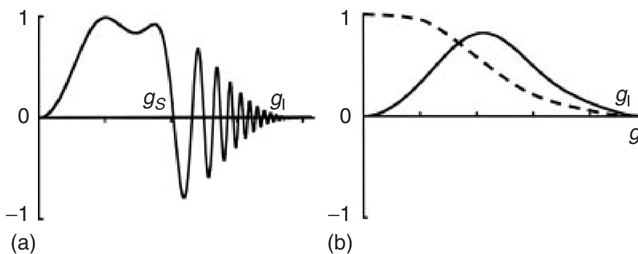

Figure 3.1 The value of the phase contrast transfer function (PCTF) as function of spatial frequency g. (a) Plot of $-\sin 2\pi\chi(\mathbf{g})$ under Scherzer conditions for an uncorrected microscope. $\chi(\mathbf{g})$ is the wave aberration function (Eq. (3.5)). g_S marks the Scherzer point resolution, g_I is the information limit defined by the spatial frequency where contrast damping due to partial temporal coherence drops to a value of $1/e^2$. (b) Plot of $\sin 2\pi\chi(\mathbf{g})$ (solid line) for NCSI conditions in an aberration-corrected instrument (see text). The region of optimized contrast expands up to the information limit. Note the bell shape indicating that transfer is far from ideal. The amplitude contrast transfer function $\cos 2\pi\chi(\mathbf{g})$ is also given (broken line).

Table 3.1 Typical optimum values for the spherical aberration parameter $Cs_{,opt}$, the defocus parameter Z_{opt}, and the radius of the point spread function R_{opt}, calculated by employing Eqs (3.7) to (3.9) for the electron energy E and the information limit g_I.

E (keV)	g_I^{-1} (nm)	$C_{S,opt}$ (μm)	Z_{opt} (nm)	R_{opt} (nm)
200	0.12	31.0	−10	0.07
300	0.07	7.5	−4.5	0.04
300	0.05	1.9	−2.3	0.03

kept as narrow as possible. There is a trade-off in the sense that increasing g_I is widening the low-spatial-frequency gap. The optimal settings for phase contrast in an aberration-corrected instrument are then given by

$$C_{S,opt} = +\tfrac{64}{27}\left(\lambda^3 g_I^4\right)^{-1} \tag{3.7}$$

$$Z_{opt} = -\tfrac{16}{9}\left(\lambda g_I^2\right)^{-1} \tag{3.8}$$

$$R_{opt} = \tfrac{16}{27} g_I^{-1} \tag{3.9}$$

Values for $C_{S,opt}$, Z_{opt}, and R_{opt} are given in Table 3.1. With typical values of 0.5–1.2 mm for C_S in an uncorrected instrument, it is evident that the residual values required for optimal contrast are only a small percentage of the original C_S values. A corresponding treatment including variable fifth-order spherical aberration is given by Lentzen [25].

We point out that the PCTF for the aberration-corrected case has a shape that is far from ideal. Admittedly, the transfer function does not show any zeros or oscillations and thus fulfills one of the central goals of constructing aberration-corrected optics. However, the transfer is very sensitively dependent on spatial frequency. Recalling that microscopy is essentially a two-Fourier transform process, we have to keep in mind that the microscope acts as a highly nonlinear filter, with the consequence that the images are formed on the basis of a wave field severely modified by inadequate contrast transfer. A number of contrast artifacts have been reported in the literature, which can be traced back to the particular shape of the PCTF [7, 26]. In another case, it was found that the width of the low-spatial-frequency gap that has to be tolerated in order to maximize g_I is too high to allow imaging of effects of chemical-bonding-induced charge redistributions in nitrogen-doped graphene [27]. All these cases indicate that high-resolution imaging is incomplete without taking focal series (whereby the region of low-contrast transfer at low spatial frequencies can be reduced) and performing a numerical backward calculation from images to structure.

3.2.3 Enhanced Contrast under Negative Spherical Aberration Conditions

So far the treatment of Lentzen *et al.* [6] is still conservative with respect to the direction of the Zernike phase shift adjusted to induce contrast. This means that under the conditions of Eqs. (3.7) and (3.8) positive phase contrast is obtained by combining a positive value of C_S with an objective lens underfocus (negative value of Z). In the following, we shall demonstrate that much improved contrast can be obtained for a wide range of imaging conditions inverting the sign of the terms in Eqs. (3.7) and (3.8.) This yields atom positions appearing bright on a dark background. According to the above definition, this is ''negative phase contrast.'' It is brought about by an overcompensation of the original value of the spherical aberration of the objective lens, that is, the contrast is due to imaging under negative spherical-aberration conditions.

This will be illustrated via image simulations for the case of strontium titanate ($SrTiO_3$). The material has a cubic perovskite structure with a lattice parameter of 0.3905 nm. Figure 3.2a shows a perspective view of the unit cell. Figure 3.2b displays the projection along the [110] crystal direction. In this viewing direction, three types of atomic columns are distinct, which are occupied alternatively with strontium and oxygen, with titanium, and with oxygen atoms. Figure 3.3 shows an experimental image taken along the [110] direction. All atomic positions are visible, including oxygen. Before, oxygen could never be seen directly in electron microscopic images. It was only accessible via the exit-plane wave function reconstruction technique [28–30]. Figure 3.4 shows simulated images for C_S values of 0 (a), +40 μm (b), and −40 μm (c) for different defocus values (horizontal axis) and sample thicknesses (vertical axis) at an electron energy of 200 keV [20].[2] Figure 3.4d shows a comparison

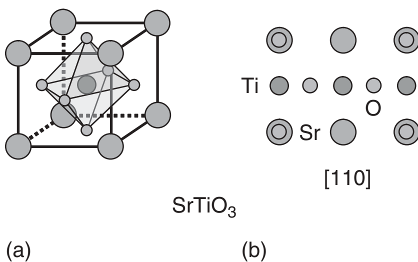

Figure 3.2 $SrTiO_3$. (a) Perspective view of the unit cell. (b) Projection along the [110] crystal direction. In this viewing direction, three types of atomic columns are distinct, which are occupied alternatively with strontium and oxygen, with titanium, and with oxygen atoms.

2) All images were calculated with the electron beam parallel to the [110] zone axis using the MacTempas software package.

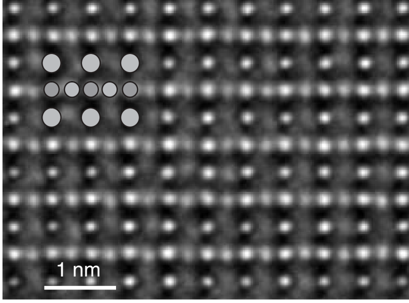

Figure 3.3 Experimental image of $SrTiO_3$ taken along the [110] zone axis employing the NCSI technique (FEI Titan 80–300 with imaging corrector, operated at 300 keV). All three atomic species are visible (compare inset) at bright contrast on a dark background.

of positive C_S combined with underfocus and negative C_S combined with overfocus. Clearly, oxygen cannot be imaged in positive phase contrast, meaning that this setup does not supply us with full atomic details in spite of the fact that the optical resolution of about 0.12 nm is sufficient to resolve the oxygen–titanium atom separation of 0.138 nm. The enhanced contrast under NCSI conditions is obvious.

Within the framework of the WPO, approximation inverting the sign of $C_{S,opt}$ and Z_{opt} changes the contrast from positive to negative phase contrast but does not yield any contrast enhancement. This can be concluded when comparing Figure 3.4b,c for very small specimen thicknesses for which the WPO approximation can be considered adequate. In order to arrive at an understanding of the contrast enhancement, two assumptions of the linear contrast theory have to be abandoned. The first is the WPO approximation. In fact, calculating the phase angles and amplitudes for different reflections for $SrTiO_3$, we find that for realistic sample thicknesses this approximation is inadequate and only a fully dynamical treatment of the electron scattering and imaging problem can provide an adequate description. Furthermore, we have to discuss *amplitude contrast*, which so far was entirely neglected.

In order to estimate the change in phase contrast intensity predicted by an expansion of the WPO treatment to the case of a "not so weak" object, we write for the wave function in the object plane

$$\psi_{obj}(\mathbf{r}) = \psi_0 + \pi i \lambda U(\mathbf{r})\, t \tag{3.10}$$

where $U(\mathbf{r})$ denotes the projected crystal potential and t the specimen thickness. This is altered by the application of the phase plate to the exit wave. Thus we obtain in the image plane,

$$\psi_{im}(\mathbf{r}) = \psi_0 \mp \pi \lambda U(\mathbf{r})\, t \tag{3.11}$$

employing a coefficient of $+i$ for positive phase contrast and $-i$ for negative phase contrast. For the "not so weak" object we maintain the intensity calculation terms

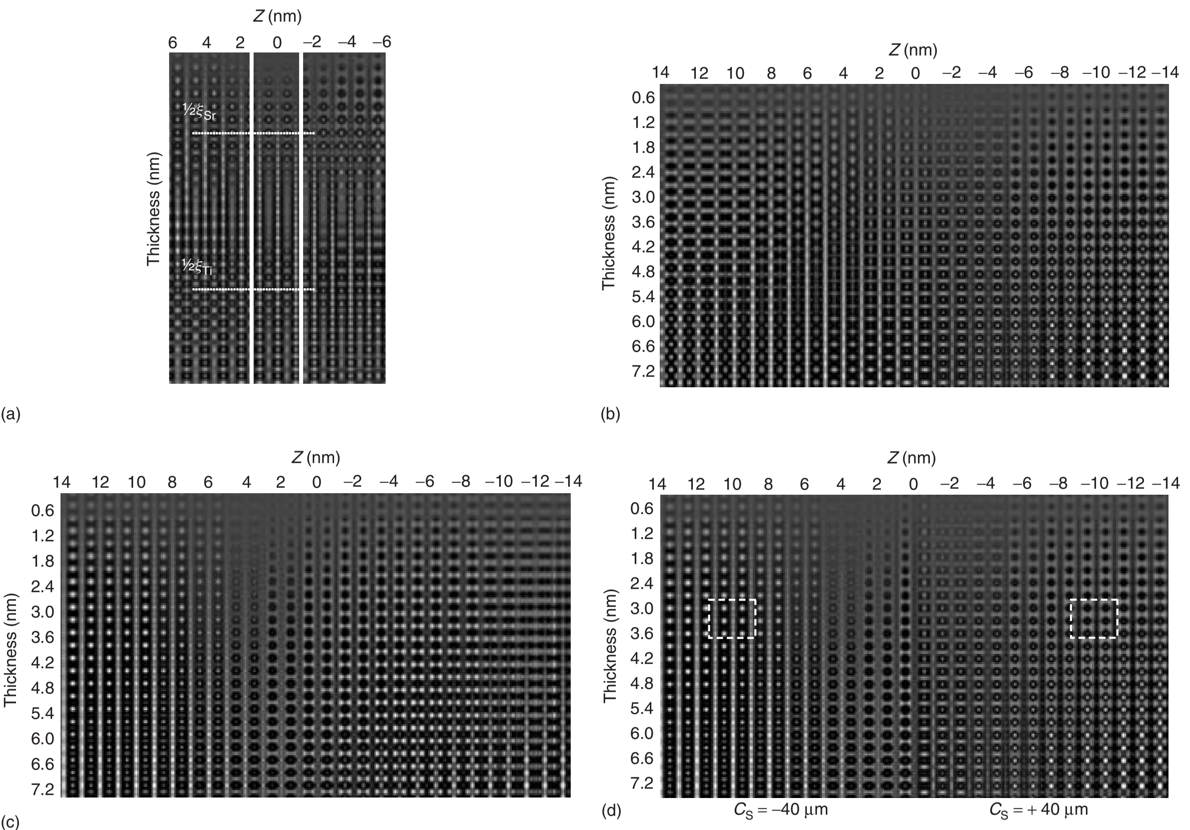

Figure 3.4 Simulated images for $SrTiO_3$ [110] at 200 keV. The composite shows a single unit cell in [110] projection for different defocus values Z and sample thicknesses at an electron energy of 200 keV for the spherical aberration parameter $C_S =$ 0 nm, +40 μm, and −40 μm (a–c). (d) Direct comparison of the positive and negative C_S situation, where in the $-C_S$ case overfocus (positive values of Z) and in the positive C_S case the usual underfocus (negative values of Z) is applied. The frame is used as a guide for the eye for same sample thickness.

up to second order, that is,

$$I(\mathbf{r}) = \psi_0^2 \mp 2\pi\psi_0\lambda U(\mathbf{r})\,t + (\pi\lambda U(\mathbf{r})\,t)^2 \tag{3.12}$$

A common phase of ψ_0 and $\psi_{sc}(\mathbf{r})$ has been chosen to set ψ_0 to a real value. The comparison of these two cases shows that the linear contribution and the quadratic contribution have different signs for positive phase contrast. The local intensity modulation at an atom column site becomes weaker on increasing the strength of the object. On the other hand, the linear contribution and the quadratic contribution have the same sign for negative phase contrast, and the local intensity modulation at an atom column site becomes stronger. In other words, setting up a negative value of spherical aberration combined with an overfocus enhances the atomic phase contrast compared to a setting with positive spherical aberration and underfocus.

Now to amplitude contrast: if the exit-plane wave function has a locally varying amplitude structure, consequentially amplitude contrast occurs. In the classic contrast treatments (e.g., [13]), only amplitude changes due to electron absorption are considered. This is not what we are dealing with. As we shall see, amplitude structure occurs for crystalline specimens as a result of electron diffraction channeling, that is, because of the elastic quantum mechanics inside the specimen. In the linear theory, amplitude contrast is proportional to $\cos 2\pi\chi(\mathbf{g})$, the amplitude contrast transfer function (ACTF). Therefore, in the case of $\chi(\mathbf{g}) = 0$, that is, full compensation of spherical aberration and zero defocus, no phase contrast but optimal amplitude contrast occurs. The ACTF for NCSI conditions is displayed schematically in Figure 3.1b.

For more insight into amplitude contrast in crystalline specimens, we neglect phase contrast for the moment, that is, we carry out a contrast calculation for $C_S = 0$ and $Z = 0$. For defect-free ideal crystals, we can perform a Bloch wave calculation. This approach is taken in the classic treatment of electron diffraction channeling [31–33]. Electron diffraction channeling describes phenomenologically an oscillatory motion of the electrons as schematically depicted in Figure 3.5 for three different sample thicknesses. This can be understood as follows. At the specimen entrance surface, the electrons are spatially uniformly distributed. While the wave field penetrates into the specimen, the positively charged atom strings interact with the electrons, attractively concentrating the electrons after some distance from the entrance surface on the atom positions. Subsequently the electrons fan out again yielding an electron current density distribution after a certain distance, which is similar to that at the surface.

In the Bloch wave formalism, it is straightforward to calculate the extinction distance

$$\xi = \left(k^{(i)} - k^{(j)}\right)^{-1} \tag{3.13}$$

where $k^{(i)}$ and $k^{(j)}$ denote the eigenvalues of the two most excited Bloch states [13]. Solving the corresponding eigenvalue problem for 200 keV electrons, we find $\xi_{SrO} \approx 14$ nm for a SrO atom column and $\xi_{Ti} \approx 38$ nm for a Ti column. Comparing this result with the atom column intensities displayed in Figure 3.4a, we find that

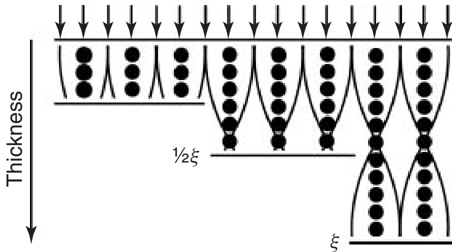

Figure 3.5 Schematic illustrating the effect of electron diffraction channeling on the local electron current density distribution for three different sample thicknesses. At the sample entrance surface, the current density distribution is assumed to be laterally uniform. The charged atoms (the atomic potential) "focus" the electrons toward the atom strings. This leads to enhanced current density at the atom positions with a maximum at a depth of odd multiples of $\xi/2$, where ξ is the extinction distance, at the expense of the current density in between the atoms. This induces an "amplitude structure" of the sample. At large sample thicknesses the current density at the atom positions decreases again, and ideally the current density becomes uniform again at depth ξ. Note that the extinction distance depends on the atomic species forming the atom string.

the atom positions appear brightest at depths of odd multiples of half the extinction distance, that is, at about 7 nm for Sr and at about 19 nm for Ti. For oxygen, the extinction distance is so large that for the moderate sample thicknesses used in high-resolution work, the intensity of oxygen atom spots in the images is always in the increasing-intensity range. This means that at $C_S = 0$ and $Z = 0$, the contrast is essentially determined by amplitude contrast induced by electron diffraction channeling.

Now it becomes evident that the strong contrast under NCSI conditions is due to additive contributions of both *amplitude* and *phase* contrast. On the one hand, because of amplitude contrast the intensity increases, at moderate specimen thicknesses, at the atom positions. The negative phase contrast, leading to bright-atom contrast at these positions too, further enhances the intensity there. On the other hand, the diffraction channeling effect reduces the electron density in between the atom positions. In this way the contrast is further enhanced.

3.2.4
NCSI Imaging for Higher Sample Thicknesses

In the previous section, we have demonstrated that the enhancement of contrast gained by adjusting the spherical-aberration parameter to a negative value and combining it with an overfocus arises from an additive contribution of bright phase contrast and bright amplitude contrast. However, the sign of phase contrast depends on sample thickness. Assuming for simplicity a case of a primary incident beam and a single scattered beam, the phase of the scattered beam at small sample thickness starts with $\pi/2$. But as the wave field advances, the specimen's scattering potential induces an additional depth-dependent phase shift. For a phase of π of the scattered beam the maximum positive phase contrast is achieved (without the

use of a Zernike phase plate). For a phase $>3\pi/2$, the contrast of the scattering centers changes from dark to bright since at this angle the vectors of the primary beam and the scattered beam are additive. The increase of the phase change per unit depth is proportional to the scattering potential. As a consequence, in order to always obtain optimal positive or negative phase contrast, a sample-thickness- and nuclear-charge-dependent pair of values for the spherical-aberration parameter and the defocusing has to be adjusted. We point out that this is not a particular property of NCSI. As soon as the advancement in the phase of the scattered beam is taken into account, optimal contrast always requires optimization of the aberration function, which means that constructing the equivalent of a Zernike phase-shift plate, advancing the phase in such a way that a total phase shift of $(2m-1)\pi/2$ is achieved with respect to the primary beam, where m is an odd integer for positive phase contrast and an even integer for negative phase contrast. The optimal conditions for bright-atom contrast have been studied by Lentzen [7] in the framework of a simple independent-atom string model for describing the diffraction channeling effect [34]. In the following, we present a brief sketch of this treatment.

The electron wave $\psi_e(\mathbf{r})$ at the exit plane of the specimen is written as the sum of a direct, unscattered wave ψ_0 and a scattered wave $\psi_s = \psi_e(\mathbf{r}) - \psi_0$. Properly adjusting the aberration function of the objective lens, a constant phase $-2\pi\chi_0$ is added to the phase of the scattered wave, which is equivalent to the action of the Zernike phase plate. Then the wave function in the image plane $\psi_i(\mathbf{r})$ can be written as

$$\psi_i(\mathbf{r}) = \psi_0 + (\psi_e(\mathbf{r}) - \psi_0)\exp(-2\pi i\chi_0) \tag{3.14}$$

Optimal contrast is obtained for the following settings for the defocus

$$Z = \frac{8\chi_0}{\lambda g_I^2} \tag{3.15}$$

and the spherical aberration parameter

$$C_S = -\frac{40\chi_0}{3\lambda^3 g_I^4} \tag{3.16}$$

In the framework of the independent-atom string model, the expressions for the direct and the scattered waves, respectively, are

$$\psi_0 = \cos\tau + i\left(\frac{U_0}{k}\xi - 1\right)\sin\tau \tag{3.17}$$

$$\psi_s = i\frac{(U(\mathbf{r}) - U_0)\,\xi}{k}\sin\tau \tag{3.18}$$

$\tau = \pi t/\xi$, and the modulus of the wave vector $k = 1/\lambda$. $U(\mathbf{r})$ is related by the scattering potential $V(\mathbf{r})$ via $U(\mathbf{r}) = 2me/h^2 V(\mathbf{r})$, with U_0 and e denoting the mean inner potential and the elementary charge, respectively. Defining the characteristic parameter

$$c = \frac{U_0\xi}{k} - 1 \tag{3.19}$$

the image intensity distribution for coherent illumination becomes

$$I(\mathbf{r}) = |\psi_i|^2 = \cos^2\tau + c^2\sin^2\tau - 2\frac{(U(\mathbf{r}) - U_0)\,\xi}{k}\sin\tau \\ \times \operatorname{Im}\left((\cos\tau - ic\sin\tau)\exp(-2\pi i\chi_0)\right) \\ + \left(\frac{U(\mathbf{r}) - U_0}{k}\right)^2 \sin^2\tau \tag{3.20}$$

The first term is the intensity of the direct wave providing uniform background intensity. The second term describes the linear interference between the direct and the scattered wave. The last term describes the intensity of the scattered wave. The maximum contrast at the atom positions occurs if the modulus of the expression in the second line adopts a maximum value and if its sign is opposite to that of $\sin\tau$. For the aberration interval of $-\frac{1}{2} < \chi_0 < \frac{1}{2}$both conditions are met for

$$\tan 2\pi\chi_0 = (c\tan\tau)^{-1} \tag{3.21}$$

and

$$\tan\tau\,\sin 2\pi\chi_0 > 0 \tag{3.22}$$

For a given material, the optimal contrast condition is then obtained employing the proper values for U_0 and ξ by calculating the value of the characteristic parameter c and solving Eq. (3.21) for χ_0 subject to fulfilling the condition Eq. (3.22). Both electron diffraction channeling and the image intensity have a thickness period equal to ξ. The phase of the scattered wave with respect to the direct wave starts with $\pi/2$ (corresponding to $\lambda/4$). It remains positive in the first half of the extinction period and turns negative in the second half, approaching $-\pi/2$ at ξ. For $c < 0$, the phase increases in the first half of the extinction period from $\pi/2$ to π and in the second half from $-\pi$ to $-\pi/2$. For $c > 0$, the phase decreases in the first half of the extinction period from $\pi/2$ to 0 and in the second half from 0 to $-\pi/2$. The conditions Eqs. (3.21) and (3.22) determine how the equivalent of the Zernike phase plate compensates the phase of the scattered wave favorably (Figure 3.6). For the first half of the extinction period χ_0 is positive; for the second half it is negative. Hence the approximation of the Zernike phase plate by defocus and spherical aberration, Eqs. (3.14) and (3.16), yields an overfocus combined with a negative value for C_S for the first half of the extinction distance and an underfocus combined with a positive C_S for the second half. Approaching a specimen thickness just smaller than half the extinction distance, the favorable compensation is achieved for $c < 0$ with a defocus

$$Z = \left(2\lambda g_I^2\right)^{-1} \tag{3.23}$$

and a value of the spherical aberration of

$$C_S = -20\left(3\lambda^3 g_I^4\right)^{-1} \tag{3.24}$$

For a specimen thickness just larger than half the extinction distance, the favorable compensation is achieved with the same settings but with the respective signs

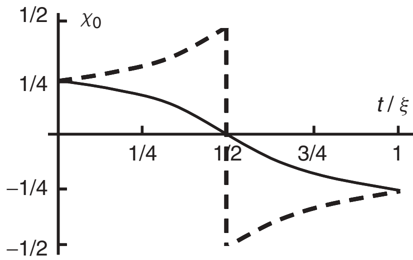

Figure 3.6 Optimal value of the aberration function χ_0 (see text) compensating the phase of the scattered wave in order to obtain maximum bright phase contrast for different sample thicknesses t in units of the extinction distance ξ. Adapted from Ref. [7].

inversed. For $c > 0$, the favorable compensation at half the extinction distance is achieved with $Z = 0$ and $C_S = 0$.

We note that the theoretical treatments as well as the experiments show that the contrast conditions are rather robust with respect to a variation of defocus and specimen thickness. We further note that the adjusted value of C_S also can vary over a wide range. Even a deviation of 30% of the calculated optimal value does not destroy the high-resolution contrast, although it certainly changes the absolute contrast behavior. The robustness of the bright-atom contrast conditions with respect to variations of C_S, Z, and t can be explained in the two-level channeling model described above by the relatively weak phase variation of the scattered wave and by the tolerance limits for the respective aberration settings [3, 35]. Although the absolute values of the imaging parameters are important for quantitative contrast evaluation, the NCSI mode *per se* does not make high demands with respect to the adjustment of particular values of these parameters.

3.3
Inversion of the Imaging Process

The images obtained in the transmission electron microscope with or without aberration-correcting optics do not generally supply us with the wanted information on the atom positions. In order to exploit the full potential of aberration-corrected atomic-resolution electron microscopy, the numerical inversion of this imaging process is mandatory. This has been done before and has also been the basis of high-resolution work in the pre-aberration correcting era. However, it has to be pointed out that the exactness of the involved numerical calculations has to be much higher than that considered satisfactory at times when the main interest was in crystallographic structure rather than in ultrahigh-precision individual atomic position measurements.

The inversion of the imaging process is carried out in two steps [28, 36–38]. The first is the reconstruction of the electron exit-plane wave function. In its generally applied form, this is done by employing the focus-variation technique: employing a charge-coupled device (CCD) camera, a series of (typically about 20) images is taken by varying the objective lens focus about a central value in steps, which, for example, in the work described in the following are based on an equidistant focus change of about 2 nm. These images form the set of primary experimental data that have to be corrected for the nonlinear transfer characteristics of the CCD camera employed for recording the images [39]. Such a correction is essential since the detector modulation-transfer function (MTF) has a strong effect on the experimental intensity versus spatial frequency characteristics in the images and contributes the major part to the so-called Stobbs factor [40]. The corrected set of data then forms the input for the numerical exit-plane wave function reconstruction employing one of the state-of-the art software codes employing maximum-likelihood methods.

For wave-function retrieval, the *actual* values of the optical parameters that appear in the aberration function are used in the calculation. Therefore, it is recommended to measure these aberrations employing the Zemlin tableau technique [3] not only before but also after the acquisition of the focal series of images. Since this often requires shifting the specimen location to an amorphous area or even exchanging the specimen for an amorphous test sample, it is likely that the measured aberration values deviate from those applying during image acquisition. The only way out of this dilemma is to consider the imaging itself as a quantum mechanical experiment by which the aberrations can be measured as long as we have a structure the precise atomic coordinates of which are known. In reality this means that we have to carry out a full and self-consistent run of the whole image-process inversion in which the exit-plane wave function is calculated with the residual aberrations taken as free parameters.

As opposed to a widespread assumption in the literature, the reconstructed ψ_e does not in general supply us with a direct representation of $\mathbf{X}$, the set of atomic coordinates. Mapping of neither the real nor the imaginary part of ψ_e gives us unambiguously the correct atomic sites. As described in the previous sections, depending on the sample thickness, the contrast varies dramatically and in a complex fashion, which cannot be understood intuitively. Furthermore, the ψ_e obtained is the wave function of the ‘‘real’’ case. This means that a tilted specimen yields as a result a ‘‘tilted’’ wave function, and the amplitude and phase distributions are those of the ‘‘real’’ case, that is, they depend on the actual specimen thickness. Of course, the set of wanted coordinates $\mathbf{X}$ must be universal and therefore independent of these rather arbitrary imaging circumstances. Therefore, as long as the imaging parameters are not precisely known, the reconstructed wave function is not yet sufficient for picometer precision microscopy. This means that the backward calculation has to be continued by performing the second step. As usual, this is done by choosing a first-guess model for which the relativistically corrected Schrödinger equation is solved to obtain the exit-plane wave function. Since neither

the sample thickness nor the beam tilt is in general known with sufficient accuracy, these have to be introduced as free parameters in an iterative fit of the model in order to reach an optimal match between calculated and experimental exit-plane wave functions. Only after a self-consistent set of atomic coordinates and imaging parameters is obtained may we consider the problem solved.

The inversion of the imaging process as it was just described looks rather canonical. Nevertheless, concerning picometer precision electron microscopy, there are issues that have to receive much greater attention than was standard in the past. First of all, it is quite likely that the original set of images is affected by small residual aberration values; in particular, this holds true for *twofold astigmatism* and *coma*. These have to be corrected in the backward calculation by expanding the iteration to comprise both steps. Another problem to be tackled is the limited precision of the alignment of the direction of the incident electron wave field with a principal low-index crystal direction. Neither the angular sensitivity of the intensity distribution in the diffraction pattern nor that in the image is sufficiently high for a precise adjustment of sample orientation. In addition, there are technical limits of even the best specimen goniometers available today, and there is always a risk of local specimen bending. Therefore, specimen tilting angles in the order of about 10 mrad can hardly be avoided. On the other hand, for realistic sample thicknesses, specimen tilts in the order of 1 mrad result in projection-related geometrical distortions of the atomic images affecting the precision of the atom position measurements. Moreover, the observable shifts of the contrast maxima inside unit cells containing different atom species cannot simply be related to each other by means of a purely geometrical factor representing the effect of the tilting angle. This can be explained by nuclear-charge dependence of electron diffraction channeling and of the corresponding shift of atomic maxima on specimen tilt. An example is given in Figure 3.7. If not properly taken into account in the numerical calculations, these different shifts of the contrast maxima for the same specimen tilting angle will lead to erroneous results. This is just another case that shows that the images, even when they resemble so closely the projected crystal structure as is the case in Figure 3.7, are not really images in the conventional sense. Only after a proper deconvolution by inversion of the two-step image formation process are our results representative of the actual atomic structure.

In the past, quantum mechanical and optical image calculations concentrated mainly on the strong atomic maxima in the images. This may be sufficient for structure investigations that concern, as already mentioned, a collective nonlocal property. But for investigations concerning individual atom column properties, this is in general not sufficient, and beyond that this would mean that we give away valuable information. Figure 3.8 shows experimental and matching simulation results concerning the behavior of the diffuse background intensity in the micrographs on changing the sample thickness and the specimen tilt. We find that the effect of tilting angles as low as 0.5 mrad can be readily detected and thus be taken into account in order to be able to realize picometer precision.

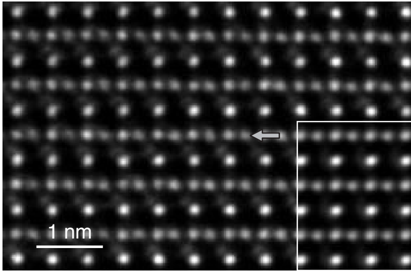

Figure 3.7 NCSI image of a $SrTiO_3$ sample taken under conditions (300 keV) where the direction of the incident electron wave field is tilted by about 7 mrad with respect to the crystallographic [110] direction. The resulting shifts of the SrO, Ti, and O atom positions (arrow) in the image are substantially different. Note that the vertical Ti atom row is no longer colinear with the SrO atom rows and that the horizontal position of a given O atom (arrow) is no longer in the exact center between the two neighboring Ti atoms. This means that the arrangement of contrast maxima in the image cannot be related in a simple way to the geometrically projected atom structure. The inset (right) was calculated for $Z = 3.0\,\text{nm}$, $t = 8.3\,\text{nm}$, $C_S = -15\ \mu\text{m}$, tilting angle 7 mrad, coefficient of twofold astigmatism $A_1 = 3\,\text{nm}$, of threefold astigmatism $A_2 = 40\,\text{nm}$, and of coma $B_2 = 30\,\text{nm}$; see Ref. [3].

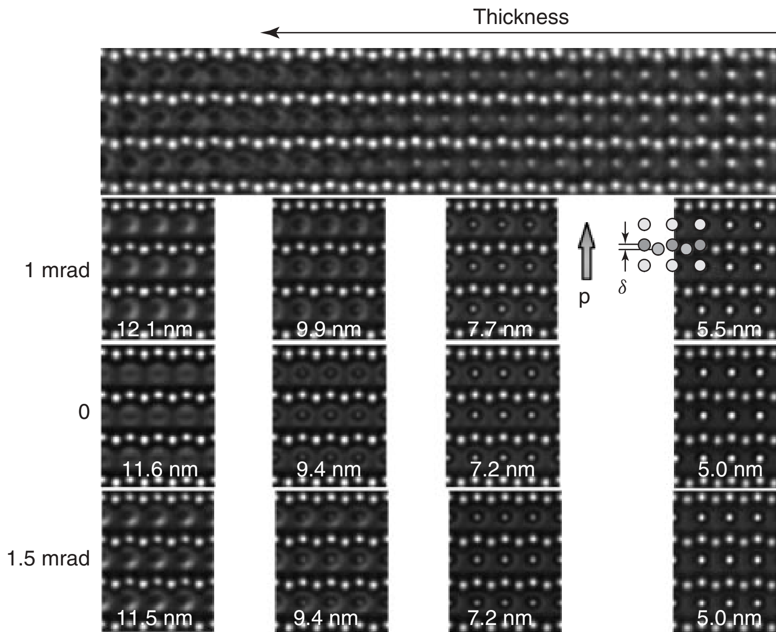

Figure 3.8 Experimental and matching simulation results concerning the behavior of the diffuse background intensity in the micrographs on changing the sample thickness and the specimen tilt (300 keV). The effect of tilting angles as low as 0.5 mrad can be readily detected and thus be taken into account in a high-quality image calculation.

3.4
Case Study: $SrTiO_3$

For quantitative atomic-resolution work it is mandatory to have an adequate optical resolution available in order to be able to separate closely spaced atom columns. Once these columns are separated, it is no longer the resolution that counts but the *precision* at which the position of an atom column or its lateral shift can be measured. Depending on the achieved signal to noise ratio of the images, this precision can be better by more than an order of magnitude than the optical resolution [41–43].

In the following, we compare by image simulations the conventional imaging mode employing a positive value of the spherical aberration coefficient (PCSI) with that achieved under NCSI conditions with respect to the obtained contrast and measurement precision of atomic column positions [44]. The images were calculated for an aberration-corrected 300 kV instrument employing optical imaging parameters for an instrumental information limit close to 0.08 nm [6, 35, 24]. Optimal NCSI contrast is obtained under these conditions (compare Section 3.4) with a spherical aberration value of $C_S = -15$ μm in combination with a defocus value of $Z = +6$ nm. The calculated intensity values were corrected on the basis of the measured actual CCD camera MTF. In addition, the effect of small electronic and mechanical instabilities of the instrument was taken into account by an image convolution using a Gaussian vibration function with a 1/e width of 0.03 nm.

Figure 3.9 shows a thickness series of images calculated for the two alternative imaging modes. The NCSI mode leads to bright-atom contrast on a dark background. This contrast is preserved up to a sample thickness of 7.7 nm and beyond. On the other hand, the PCSI mode results in dark atom contrast for relatively thin objects ($t < 4.4$ nm), while bright peaks appear at the Sr atom positions for higher thicknesses. For a quantitative comparison, the images are normalized to a mean intensity of 1, such that the standard deviation of the intensity reflects the image contrast. Figure 3.10 displays the image contrast as a function of thickness. The contrast resulting from the two modes exhibits the same value at an object thickness of 1.1 nm. In the case of the NCSI mode, the contrast grows with increasing thickness up to about 5 nm, reaching a saturation value of about 0.27. The contrast increase of the PCSI mode is much lower, and a saturation plateau already occurs in the thickness region between 3 and 7 nm. For the thickness range of 3–7 nm typical for high-resolution work in $SrTiO_3$, the NCSI contrast is on average stronger by about a factor of 2 than the PCSI contrast. We note that this comparison neglects the fact that under PCSI conditions and larger sample thicknesses the different atom species appear at different contrasts (bright on a dark background for Sr and complicated gray-scale contrast for Ti and O), which is not very convenient for quantitative studies, in particular, those where measurements on Ti and O are intended.

The obtainable signal to noise ratio depends directly on the image intensity recorded at an atomic column position and determines the precision of position and occupancy measurements. The intensity values for the three types of columns,

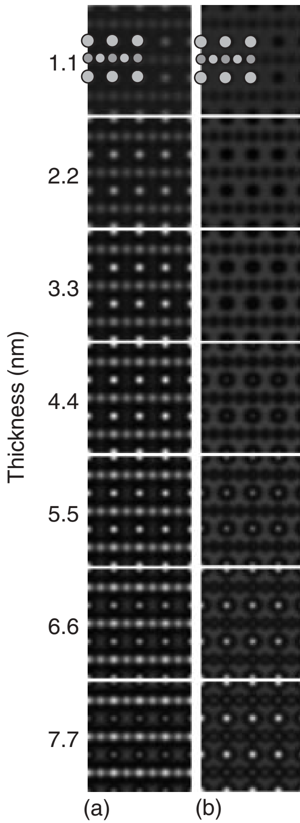

Figure 3.9 Simulated thickness series of images calculated for the negative spherical-aberration imaging (NCSI) mode (a) and the conventional PCSI imaging mode (b). The NCSI mode leads to bright-atom contrast on a dark background. This contrast is preserved up to a sample thickness of 7.7 nm and beyond. PCSI conditions result in dark atom contrast for relatively thin objects ($t < 4.4$ nm), while bright peaks appear at the Sr atom positions for higher thicknesses. In the upper part of the figure, the atom positions of $SrTiO_3$ are given schematically [44].

SrO, Ti, and O are plotted in Figure 3.11 for a sample thickness of 3.3 nm. At this thickness, the image taken under PCSI conditions has essentially reached its plateau contrast level, while the already much superior contrast level in the NCSI case increases further at larger thickness. Figure 3.11a shows the signal intensity associated with the SrO columns, and Figure 3.11b, the intensity of the Ti and O columns. The mean intensity one is denoted by a dotted line. For a quantitative comparison, the ratio of the column-based signal strength between the two imaging modes is defined by the ratio of the respective intensity extrema at the column positions, given by $(I_{max} - 1)_{NCSI}/(1 - I_{min})_{PCSI}$. The calculated results are 3.6 for SrO, 2.4 for Ti, and 2.1 for O. These ratios of the extremal values

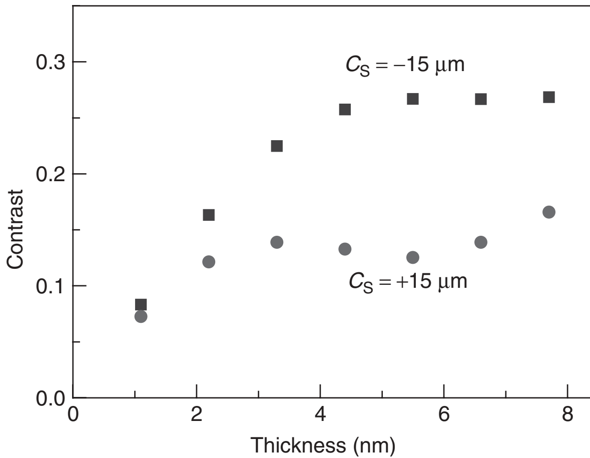

Figure 3.10 The image contrast (defined by the standard deviation from the mean intensity) as a function of specimen thickness. In the case of NCSI (squares), the contrast is growing with increasing thickness up to about 5 nm, where it reaches a saturation value of about 0.27. The contrast increase of the PCSI mode (filled circles) is much lower, and saturation occurs already in the thickness region between 3 and 7 nm [44].

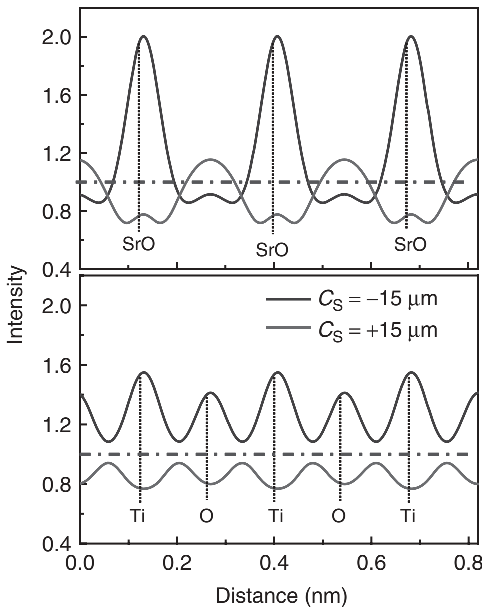

Figure 3.11 Plot of the intensity values for SrO, Ti, and O atom positions for a sample thickness of 3.3 nm. High-amplitude black line: NCSI. Low-amplitude grey line: PCSI. The mean intensity 1 is denoted by a dotted line [44].

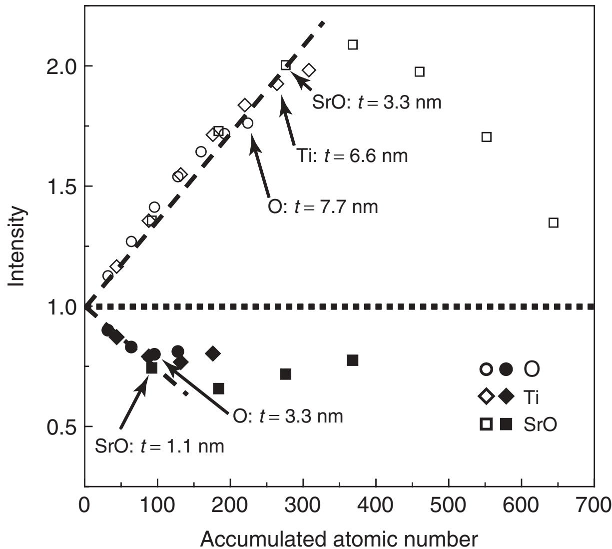

Figure 3.12 Dependence of the image intensity on the atomic number accumulated per individual atomic column along the viewing direction. Along the [110] direction, a unit cell period of $SrTiO_3$ includes one strontium plus one oxygen atom in the SrO column, one titanium atom in the Ti column, and two oxygen atoms in the oxygen column. The atomic numbers accumulated over a single unit cell period are thus 46 (SrO), 22 (Ti), and 16 (O), respectively [44].

between the NCSI and the PCSI modes are for all individual column types even larger than the corresponding ratio of the overall image contrast of 1.6. This reflects the much stronger ‘‘focused’’ shape of the atomic column images in the NCSI mode.

Figure 3.12 shows the dependence of the image intensity on the atomic number accumulated per individual atomic column along the viewing direction. It is noted that along the [110] direction, a unit cell period of $SrTiO_3$ includes one strontium plus one oxygen atom in the SrO column, one Ti atom in the Ti column, and two oxygen atoms in the oxygen column. The atomic numbers accumulated over a single unit cell period are thus 46, 22, and 16, respectively. For the NCSI mode, the image intensity of all columns follows essentially a linear dependence on the total atomic number accumulated up to a thickness of at least 3.3 nm. Beyond this thickness, the linear relation is still valid for the lighter Ti and O columns, whereas the linearity is lost for the SrO columns because of their shorter extinction length. In the case of the PCSI mode, the linearity between column intensity and the accumulated atomic number is already lost for all column types at a thickness of 3.3 nm. Most importantly, the linear dependence of the column intensity on the accumulated atomic number exhibits also a higher slope in the NCSI mode than in PCSI mode.

3.5 Practical Examples of Application of NCSI Imaging

The first atomic-resolution studies employing the NCSI technique were carried out in $SrTiO_3$ and in $YBa_2Cu_3O_7$ [8]. Subsequently, the technique was employed to measure the oxygen occupancy in $\Sigma 3\{111\}$ twin boundaries in $BaTiO_3$ thin films [45]. Further studies employing the NCSI technique concerned the reconstructed 90° tilt grain boundary in $YBa_2Cu_3O_7$ [43], the atomic structure of the core of dislocations in $SrTiO_3$ [46, 47], of defects in GaAs [48] and of the Si/$SrTiO_3$ interface [49]. Using NCSI, the stability and dynamics of graphene were studied [50]. The effect of a single dislocation in the $SrTiO_3$ substrate on the structure of epitaxial PZT was investigated [51]. Another study employing the NCSI mode yielded the high-precision atomic structure of the interface between $SrTiO_3$ and $LaAlO_3$ [52]. A study of the core structure of dislocations in plastically deformed sapphire [53] was carried out, and the atomic surface termination, structural relaxation, and electronic structure of the polar (111) surface were investigated in Co_3O_4 [54]. Mapping the polarization dipole distribution measured by atom position measurements of Ti and O atoms close to a PZT/$SrTiO_3$ interface allowed demonstration that closure-domain structures closing the electric flux by continuous dipole rotation occur in ferroelectrics [55].

For illustration, we reproduce here the results of the study on the atomic structure of 180° inversion domain walls in PZT, that is, $Pb(Zr_{0.2}Ti_{0.8})O_3$ [56]. PZT is a widely used technical ferroelectric, used, for instance, in the form of thin films in ferroelectric memories. Data storage is performed by switching the ferroelectric polarization. The polarization state migrates through the specimen, and areas of different polarization are separated by domain walls in which the state of polarization changes from one direction to the other. Figure 3.13 displays an NCSI electron micrograph of PZT sandwiched between two $SrTiO_3$ layers. The insets are magnifications that allow identification of the individual atom species and a closer look at the particular position of the atomic sites. Evidence for the polarized state can be obtained by inspection of the individual atom positions in the unit cell. In the inset on the left, the Zr/Ti (mixed) sites are shifted toward the upper vertical Pb atom row. The oxygen atoms are shifted even further. As a result, they are no longer collinear with the Zr/Ti atom row. The situation is depicted schematically in the inset. According to definition, the polarization vector $\mathbf{p}$ points downward. In the inset at the lower right, the shifts are in the opposite direction, and as a consequence, the polarization vector is inverted. In between we have a 180° inversion domain wall (broken line).

The oblique parts of the wall are made up of transversal segments and very short longitudinal segments. They are essentially uncharged since the electric fields characterized by the polarization vectors of the adjoining boundary segments just cancel each other pair wise. In the horizontal domain-wall segments, the polarization vectors are, across the wall, meeting head to head. As a result, the electric fields do not cancel and the boundary is charged. Since we have genuine atomic resolution, we have access to each individual atomic position in this [110]

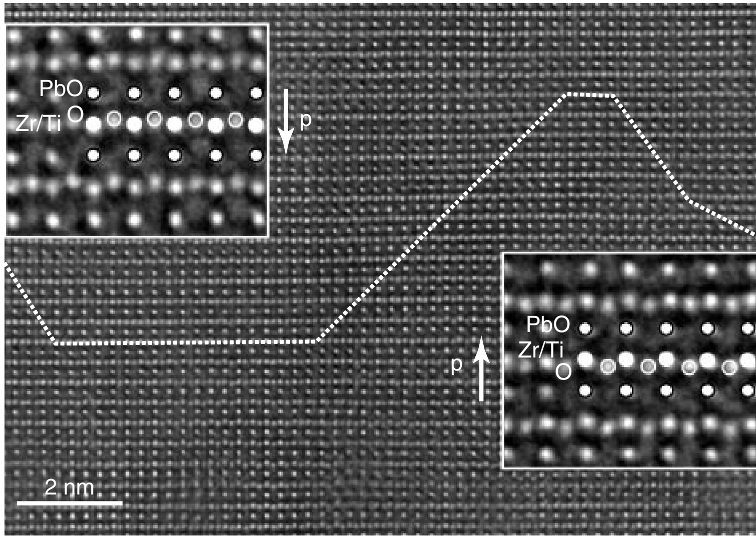

Figure 3.13 $Pb(Zr_{0.2}Ti_{0.8})O_3$ imaged along the [110] direction. The inset on the left shows that the horizontal Zr/Ti atom rows are shifted toward the respective Pb atom row above the Zr/Ti row. Oxygen is shifted even more, thus becoming no longer co-linear with the Zr/Ti rows. This indicates that the material is ferroelectrically polarized. The polarization vector **p** points downward. The inset on the right shows opposite atomic shifts. The direction of the polarization vector there is upward. The dotted line shows the appertaining ferroelectric inversion domain wall. With respect to the atomic structure, the inclined domain-wall sections consist of vertical transversal and horizontal longitudinal domain-wall segments. As a result they are uncharged. The horizontal sections are longitudinal domain walls, which are charged [56].

projection. This allows making individual measurements of the atomic shifts. It is found that the transversal walls are only a single projected unit cell thick (Figure 3.14). Figure 3.15a shows for a longitudinal domain wall the results of the measurements of the atomic shifts of the O and Zr/Ti atoms out of their symmetric positions with single-atom column resolution. The Gaussian regression analysis indicates a precision of better than 5 p.m. (for a 95% confidence level). This wall is rather extended, about 10 lattice constants. From these measurements, we can infer that this kind of domain wall reduces the field energy by increasing its width substantially over that of the charge-neutral transversal wall. Figure 3.15b shows the value of the macroscopic spontaneous polarization P_S calculated from the measured atomic shifts employing calculated values [57] for the effective charges of the ions. This demonstrates that by exploiting the potential of the atomically resolving ultrahigh-resolution techniques we can determine local physical properties such as the spontaneous polarization directly from measurements of shifts of the individual atom positions. This fulfills an old dream in materials science to be able to obtain a direct link between atomic level information and macroscopic properties.

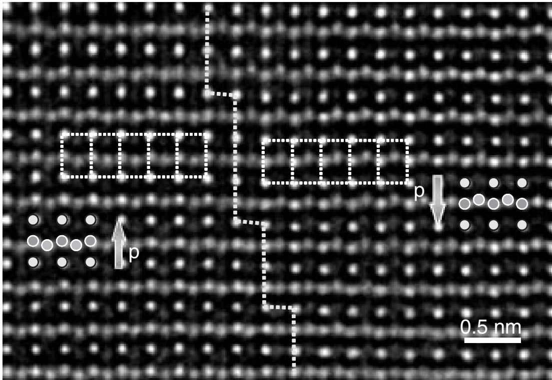

Figure 3.14 A 180° domain-wall segment of mixed type seen edge-on. The arrows ''**p**'' indicate the opposite polarization directions across the domain wall. The parallelograms denote the segments of transversal domain wall. The vertical dotted line marks the central plane of the domain wall. The horizontal dotted lines trace projected unit cells on either side of the domain wall. Indicated by the shift of the oxygen atoms, ''up'' on the left and ''down'' on the right of the central plane indicates directly that the width of the wall is a single <110> projected unit cell wide [56].

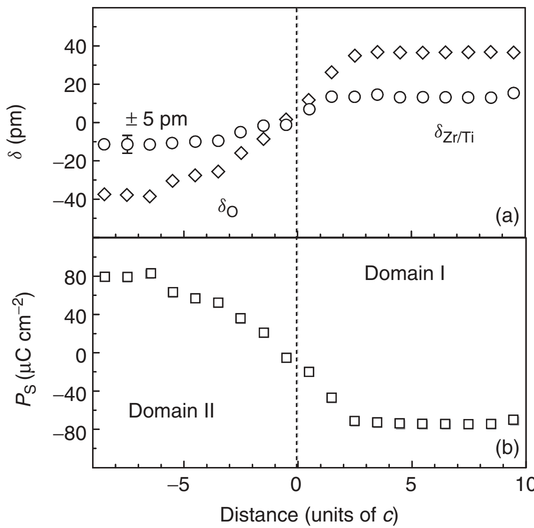

Figure 3.15 (a) Longitudinal inversion domain-wall atom shifts measured on the atomic sites and averaged for better statistics. $\delta_{Zr/Ti}$ denotes the upward shift of the Zr/Ti atom positions toward Pb (cf. inset on the left in Figure 3.13) as a function of distance (in units of the crystallographic c lattice parameter) from the domain wall center. δ_O denotes the corresponding oxygen atom shift. The domain wall width amounting to 10 unit cell distances is much wider than the transversal wall sections. This reduces the electric field energy. (b) The macroscopic spontaneous polarization P_S calculated on the basis of measuring the individual atomic shifts [56].

References

1. Rose, H. (1990) Outline of a spherically corrected semiaplanatic medium-voltage transmission electron microscope. *Optik*, **85**, 19–24.
2. Haider, M., Uhlemann, S., Schwan, E., Rose, H., Kabius, B., and Urban, K. (1998) Electron microscopy image enhanced. *Nature*, **392**, 768–769.
3. Uhlemann, S. and Haider, M. (1998) Residual wave aberrations in the first spherical aberration corrected transmission electron microscope. *Ultramicroscopy*, **72**, 109–119.
4. Scherzer, O. (1949) The theoretical resolution limit of the electron microscope. *J. Appl. Phys.*, **20**, 20–29.
5. Lichte, H. (1991) Optimum focus for taking electron holograms. *Ultramicroscopy*, **38**, 13–22.
6. Lentzen, M., Jahnen, B., Jia, C.-L., Thust, A., Tillmann, K., and Urban, K. (2002) High-resolution imaging with an aberration corrected transmission electron microscope. *Ultramicroscopy*, **92**, 233–242.
7. Lentzen, M. (2004) The tuning of a Zernike phase plate with defocus and variable spherical aberration and its use in HRTEM imaging. *Ultramicroscopy*, **99**, 211–220.
8. Jia, C.-L., Lentzen, M., and Urban, K. (2003) Atomic-resolution imaging of oxygen in perovskite ceramics. *Science*, **299**, 870–873.
9. Urban, K.W. (2008) Studying atomic structures by aberration-corrected transmission electron microscopy. *Science*, **321**, 506–510.
10. Urban, K.W. (2009) Is science prepared for atomic resolution electron microscopy. *Nat. Mater.*, **8**, 260–262.
11. Urban, K.W., Houben, L., Jia, C.-L., Lentzen, M., Mi, S.-B., Tillmann, K., and Thust, A. (2008) in *Advances in Imaging and Electron Physics*, vol. 153 (ed. P. Hawkes), Academic Press, Oxford, pp. 320–344.
12. Urban, K.W., Jia, C.-L., Houben, L., Lentzen, M., Mi, S.-B., and Tillmann, K. (2009) Negative spherical aberration ultrahigh-resolution imaging in corrected transmission electron microscopy. *Philos. Trans. R. Soc. A*, **367**, 3735–3753.
13. Reimer, L. (1984) *Transmission Electron Microscopy*, Springer, Berlin.
14. Williams, D.B. and Carter, C.B. (2009) *Transmission Electron Microscopy*, 2nd edn, Springer, New York.
15. Spence, J.C.H. (2007) *High Resolution Electron Microscopy*, 3rd edn, Oxford University Press, New York.
16. Saxton, W.O. (2000) A new way of measuring microscope aberrations. *Ultramicroscopy*, **81**, 41–45.
17. Lentzen, M. (2006) Progress in aberration-corrected high-resolution transmission electron microscopy using hardware aberration correction. *Microsc. Microanal.*, **12**, 191–205.
18. Born, M. and Wolf, E. (1999) *Principles of Optics*, 7th edn, Cambridge University Press, Cambridge, UK.
19. Stadelmann, P.A. (1987) EMS – a software package for electron diffraction analysis and HREM image simulation in materials science. *Ultramicroscopy*, **21**, 131–145.
20. Kilaas, R. (1987) in *Proceedings of the 45th Annual EMSA Meeting* (ed. G.W. Bailey), San Francisco Press, San Francisco, CA, pp. 66–67.
21. Zernike, F. (1942) Phase contrast, a new method for the microscopic observation of transparent objects, Part I. *Physica*, **9**, 686–698.
22. Zernike, F. (1942) Phase contrast, a new method for the microscopic observation of transparent objects, Part II. *Physica*, **9**, 974–986.
23. Hanszen, K.-J. and Trepte, L. (1971) The influence of voltage and current fluctuations and of a finite energy width of the electrons on contrast and resolution in electron microscopy. *Optik*, **32**, 519–538.
24. Barthel, J. and Thust, A. (2008) Quantification of the information limit of transmission electron microscopes. *Phys. Rev. Lett.*, **101**, 200801 - 1–200801-4.
25. Lentzen, M. (2008) Contrast transfer and resolution limits for sub-angström high-resolution transmission electron

microscopy. *Microsc. Microanal.*, **14**, 16–26.
26. Zhang, Z. and Kaiser, U. (2009) Structural imaging of β-Si_3N_4 by spherical aberration-corrected high-resolution transmission electron microscopy. *Ultramicroscopy*, **109**, 1114–1120.
27. Meyer, J.C., Kurasch, S., Park, H.J., Skakalova, V., Künzel, D., Groß, A., Chuvilin, A., Algara-Siller, G., Roth, S., Iwasaki, T., Starke, U., Smet, J.H., and Kaiser, U. (2011) Experimental analysis of charge redistribution due to chemical bonding by high-resolution transmission electron microscopy. *Nat. Mater.*, **10**, 209–215.
28. Coene, W., Janssen, G., Op de Beeck, M., and van Dyck, D. (1992) Phase retrieval through focus variation for ultra-resolution in field emission transmission electron microscopy. *Phys. Rev. Lett.*, **69**, 3743–3746.
29. Jia, C.-L. and Thust, A. (1999) Investigation of atom displacements at a $\sum 3$ {111} twin boundary in $BaTiO_3$ by means of phase-retrieval electron microscopy. *Phys. Rev. Lett.*, **82**, 5052–5055.
30. Kisielowski, C., Hetherington, C.J.D., Wang, Y.C., Kilaas, R., O'Keefe, M.A., and Thust, A. (2001) Imaging columns of the light elements carbon, nitrogen and oxygen with sub- Angström resolution. *Ultramicroscopy*, **89**, 243–263.
31. Howie, A. (1966) Diffraction channelling of fast electrons and positrons in crystals. *Philos. Mag.*, **14**, 223–237.
32. Urban, K. and Yoshida, N. (1979) The effect of electron diffraction channelling on the displacement of atoms in electron-irradiated crystals. *Radiat. Eff. Defects Solids*, **42**, 1–15.
33. van Dyck, D. and Op de Beeck, M. (1996) A simple intuitive theory for electron diffraction. *Ultramicroscopy*, **64**, 199–2007.
34. Lentzen, M. and Urban, K. (2000) Reconstruction of the projected crystal potential in transmission electron microscopy by means of a maximum-likelihood refinement algorithm. *Acta Crystallogr. A*, **56**, 235–247.
35. Jia, C.-L., Lentzen, M., and Urban, K. (2004) High resolution transmission electron microscopy using negative spherical aberration. *Microsc. Microanal.*, **10**, 174–184.
36. Coene, W.M.J., Thust, A., Op de Beeck, M., and Van Dyck, D. (1996) Maximum-likelihood method for focus-variation image reconstruction in high resolution transmission electron microscopy. *Ultramicroscopy*, **64**, 109–135.
37. Thust, A., Coene, W.M.J., Op de Beeck, M., and Van Dyck, D. (1996) Focal-series reconstruction in HRTEM: simulation studies on non-periodic objects. *Ultramicroscopy*, **64**, 211–230.
38. Thust, A., Overwijk, M.H.F., Coene, W.M.J., and Lentzen, M. (1996) Numerical correction of lens aberrations in phase-retrieval HRTEM. *Ultramicroscopy*, **64**, 249–264.
39. Thust, A. (2009) High-resolution transmission electron microscopy on an absolute contrast scale. *Phys. Rev. Lett.*, **102**, 220801-1–220801-4.
40. Hÿtch, M. and Stobbs, W. (1994) Quantitative comparison of high resolution TEM images with image simulations. *Ultramicroscopy*, **53**, 191–203.
41. Den Dekker, A.J., Van Aert, S., van den Bos, A., and Van Dyck, D. (2005) Maximum likelihood estimation of structure parameters from high resolution electron microscopy images. Part I: a theoretical framework. *Ultramicroscopy*, **104**, 83–106.
42. Van Aert, S., den Dekker, A.J., van den Bos, A., Van Dyck, D., and Chen, J.H. (2005) Maximum likelihood estimation of structure parameters from high resolution electron microscopy images. Part II: a practical example. *Ultramicroscopy*, **104**, 107–125.
43. Houben, L., Thust, A., and Urban, K. (2006) Atomic-precision determination of the reconstruction of a 90° tilt boundary in $YBa_2Cu_3O_7$ by aberration corrected HRTEM. *Ultramicroscopy*, **106**, 200–214.
44. Jia, C.-L., Houben, L., Thust, A., and Barthel, J. (2010) On the benefit of the negative spherical-aberration imaging technique for quantitative HRTEM. *Ultramicroscopy*, **110**, 500–505.

45. Jia, C.-L. and Urban, K. (2004) Atomic-resolution measurement of oxygen concentration in oxide materials. *Science*, **303**, 2001–2004.

46. Jia, C.-L., Thust, A., and Urban, K. (2005) Atomic-scale analysis of the oxygen configuration at a $SrTiO_3$ dislocation core. *Phys. Rev. Lett.*, **95**, 225506-1–225506-4.

47. Jia, C.-L., Houben, L., and Urban, K. (2006) Atom vacancies at a screw dislocation core in $SrTiO_3$. *Philos. Mag. Lett.*, **86**, 683–690.

48. Tillmann, K., Thust, A., and Urban, K. (2004) Spherical aberration correction in tandem with exit-plane wave function reconstruction: interlocking tools for the atomic scale imaging of lattice defects in GaAs. *Microsc. Microanal.*, **10**, 185–198.

49. Mi, S.-B., Jia, C.-L., Vaithyanathan, V., Houben, L., Schubert, J., Schlom, D.G., and Urban, K. (2008) Atomic structure of the interface between SrTiO3 thin films and Si (001) substrates. *Appl. Phys. Lett.*, **93**, 101913- 1–101913-3.

50. Girit, Ç.Ö., Meyer, J.C., Erni, R., Rossel, M.D., Kisielowski, C., Yang, L., Park, C.H., Crommie, M.F., Cohen, M.L., Louie, S.G., and Zettl, A. (2009) Graphene at the edge: stability and dynamics. *Science*, **323**, 1705–1708.

51. Jia, C.-L., Mi, S.-B., Urban, K., Vrejoiu, I., Alexe, M., and Hesse, D. (2009) Effect of a single dislocation in a heterostructure layer on the local polarization of a ferroelectric layer. *Phys. Rev. Lett.*, **102**, 117601-1–117601-4.

52. Jia, C.-L., Mi, S.-B., Faley, M., Poppe, U., Schubert, J., and Urban, K. (2009) Oxygen octahedron reconstruction in the $SrTiO_3$ / $LaAlO_3$ heterointerfaces investigated using aberration-corrected ultrahigh-resolution transmission electron microscopy. *Phys. Rev. B*, **79**, 81405(R)-1–81405(R)-4.

53. Heuer, A.H., Jia, C.-L., and Lagerlöf, K.P.D. (2010) The core structure of basal dislocations in deformed sapphire (a-Al_2O_3). *Science*, **330**, 1227–1231.

54. Yu, R., Hu, L.H., Cheng, Z.Y., Li, Y.D., Ye, Q., and Zhu, J. (2010) Direct sub-angström measurement of surfaces of oxide particles. *Phys. Rev. Lett.*, **105**, 226101-1–226101-4.

55. Jia, C.-L., Urban, K., Vrejoiu, I., Alexe, M., and Hesse, D. (2011) *Science*, **331**, 1420–1423.

56. Jia, C.-L., Mi, S.B., Urban, K., Vrejoiu, I., Alexe, M., and Hesse, D. (2008) Atomic-scale study of electric dipoles near charged and uncharged domain walls in ferroelectric films. *Nat. Mater.*, **7**, 57–61.

57. Zhong, W., King-Smith, R.D., and Vanderbilt, D. (1994) Giant LO-TO splittings in perovskite ferroelectrics. *Phys. Rev. Lett.*, **72**, 3618–3621.